RSC Advances

PAPER

View Article Online
View Journal | View Issue

Cite this: *RSC Adv.*, 2018, **8**, 6709

Effect of a pH-controlled co-precipitation process on rhodamine B adsorption of $MnFe_2O_4$ nanoparticles

Umaporn Lamdab,[a] Khatcharin Wetchakun,[b] Wiyong Kangwansupamonkon[cd] and Natda Wetchakun *[ae]

Received 22nd December 2017
Accepted 4th February 2018

DOI: 10.1039/c7ra13570j

rsc.li/rsc-advances

We investigated the effect of a pH-controlled co-precipitation process on the adsorption behavior of manganese ferrite ($MnFe_2O_4$) nanoparticles as well as their structural and magnetic properties. The pH of prepared $MnFe_2O_4$ nanoparticles is typically an important factor affecting the adsorption capacity of an adsorbent. In this study, $MnFe_2O_4$ nanoparticles were prepared using a co-precipitation method at four different pH values of 9.0, 9.5, 10.0, and 10.5. The adsorption behaviors on rhodamine B (RhB) by $MnFe_2O_4$ nanoparticles prepared at different pH values were investigated. It was found that, *via* a pH-controlled process, $MnFe_2O_4$ nanoparticles prepared at pH 10.5 showed the highest RhB removal efficiency. The results indicated that the large pore size and surface charge of $MnFe_2O_4$ nanoparticles improved the adsorption capacities for RhB. Kinetic data were fitted to a pseudo-second order kinetic model and revealed that equilibrium was reached within 60 min. The isotherm data showed that the Langmuir maximum adsorption capacity of the $MnFe_2O_4$ nanoparticles prepared at pH 10.5 for RhB was 9.30 mg g^{-1}.

1. Introduction

Many textile industries use processes, such as dyeing silk, wool, jute, leather and cotton that are major sources of severe worldwide water pollution problems.[1] The release of many dyes in the water is very harmful because these strong colored components create dangerous byproducts through oxidation, and inhibit benthic photosynthesis.[2,3] The toxic and carcinogenic degraded products of dyes from industrial effluents released into clean water affect the central nervous system in humans and the environment.[4,5] Rhodamine B (RhB), a cationic dye, is a major source of environmental pollution because of its stability and resistance to biodegradation.[6] It can be toxic to human beings and animals, and causes the irritation of skin, eyes and respiratory tract.[7,8] Thus, the development of efficient methods for RhB elimination is urgently needed. Several techniques such as advanced oxidation processes,[9,10] direct coagulation/flocculation-sand filtration or ozonation,[11–14] membrane separation,[15] coagulation and flocculation,[16] as well as adsorption,[17–19] have been used to remove dyes from wastewater. Adsorption processes are considered to be an effective, promising and economical alternative, which can be used to remove dyes in water.[20–22] Recently, magnetic nanoparticles have been used to remove dyes from water. Among ferrites utilized for dye removal, manganese ferrite ($MnFe_2O_4$) is the most prominent ferrite because of its highest magnetization, high catalytic activity, and good durability. Moreover, $MnFe_2O_4$ provides an advantage for repeating magnetic separation with good stability.[23–29] It has been shown that $MnFe_2O_4$ nanoparticles can be prepared *via* several methods such as hydrothermal,[30,31] sol–gel,[29,32] and co-precipitation.[33–35] Among these methods, co-precipitation has been widely utilized for the preparation of magnetic ferrite. When compared to other methods, the products obtained from a co-precipitation method are relatively uniform, and can be prepared easily and scaled up for industrial purposes. From previous reports, the physical properties of $MnFe_2O_4$ nanoparticles were strongly dependent on the pH preparation value.[36–38] Therefore, controlling the pH value within the co-precipitation process is important for the synthesis of $MnFe_2O_4$ nanoparticles with the desired morphology and size for efficient adsorption. To the best of our knowledge, the characteristics and adsorption properties of $MnFe_2O_4$ nanoparticles prepared at various pH values for RhB removal have not been investigated.

[a]*Department of Physics and Materials Science, Faculty of Science, Chiang Mai University, Chiang Mai 50200, Thailand. E-mail: natda_we@yahoo.com*

[b]*Program of Physics, Faculty of Science, Ubon Ratchathani Rajabhat University, Ubon Ratchathani 34000, Thailand*

[c]*National Nanotechnology Center, National Science and Technology Development Agency, 111 Thailand Science Park, Paholyothin Road, Khlong Luang, Pathumthani 12120, Thailand*

[d]*AFRST, The Royal Society of Thailand, Sanam Sueapa, Dusit, Bangkok 10300, Thailand*

[e]*Materials Science Research Center, Faculty of Science, Chiang Mai University, Chiang Mai 50200, Thailand*

In this study, the $MnFe_2O_4$ nanoparticles prepared at different pH values of 9.0, 9.5, 10.0, and 10.5 were synthesized by a co-precipitation method. The effect of controlling the pH during the co-precipitation process was studied to determine the crystal structure, morphology, magnetic properties of the $MnFe_2O_4$ nanoparticles. The adsorption capacities, adsorption kinetics and adsorption isotherms of the obtained $MnFe_2O_4$ nanoparticles were evaluated based on the efficiency of the RhB removal.

2. Experimental

2.1 Preparation of $MnFe_2O_4$ nanoparticles

$MnFe_2O_4$ nanoparticles were prepared using a co-precipitation method. Firstly, 25 mM of manganese nitrate hydrate ($Mn(NO_3)_2 \cdot xH_2O$, Sigma-Aldrich, USA, 98%) and 50 mM of iron nitrate nonahydrate ($Fe(NO_3)_3 \cdot 9H_2O$, Sigma-Aldrich, USA, 98%) were dissolved in deionized water. These solutions were mixed together using magnetic stirring at a constant speed. Then, the mixed solution was heated to 70 °C for 15 min, and then added dropwise 0.2 M of sodium hydroxide (NaOH, Sigma-Aldrich, 97%). The pH of each solution was adjusted to form different values of 9.0, 9.5, 10.0, and 10.5. Correspondingly, the $MnFe_2O_4$ samples produced during the pH-controlled preparation process were denoted as $MnFe_2O_4$-pH 9.0, $MnFe_2O_4$-pH 9.5, $MnFe_2O_4$-pH 10.0, and $MnFe_2O_4$-pH 10.5. The mixture solutions were then stirred magnetically for 24 h at room temperature. The obtained precipitates were washed with deionized water by centrifugation several times and were dried at 80 °C for 24 h. A flow diagram of $MnFe_2O_4$ nanoparticles preparation at the pH values of 9.0, 9.5, 10.0, and 10.5 by co-precipitation method are shown in Fig. 1.

2.2 Characterization

The crystal phases of all samples were characterized by X-ray diffraction (XRD, JEOL JDX-3530) with Cu K_α irradiation (λ = 1.5418 nm). The morphology and particle size were determined by scanning electron microscopy (SEM, JEOL JSM-6335F) and transmission electron microscopy (TEM, JEOL JEM-2010). The Brunauer–Emmett–Teller (BET) specific surface area and pore size of the prepared samples were analyzed by nitrogen adsorption–desorption isotherms obtained using an autosorb 1 MP (Quantachrome). The zeta potential determined by zetasizer nano instrument (ZS Malvern) was used to evaluate the isoelectric point (IEP) of the $MnFe_2O_4$ nanoparticles. A vibrating sample magnetometer (VSM, Lakeshore VSM 7400) was employed to measure the magnetic properties of the obtained samples. The Fourier transform infrared (FTIR) spectra of the samples were recorded in the 4000–400 cm^{-1} wavenumber region using KBr disks as standard on a Thermo Scientific model Nicolet 6700 FT-IR spectrophotometer. Surface composition and oxidation state were carried out using X-ray photoelectron spectroscopy (XPS, Kratos Axis ULTRA^{DLD}) with a monochromatic Al K_α source (1486.6 eV). All XPS spectra for the samples were referenced by setting the adventitious carbon C (1s) peak to 284.8 eV.

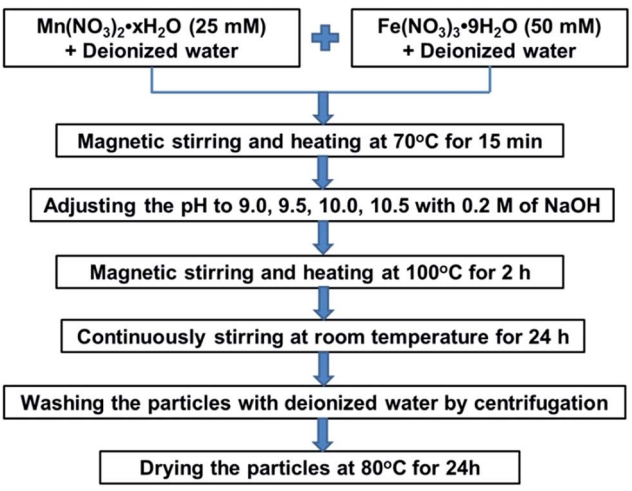

Fig. 1 Flow diagram of the $MnFe_2O_4$ nanoparticles preparation by co-precipitation at the pH values of 9.0, 9.5, 10.0, and 10.5.

2.3 Adsorption experiments

The adsorption properties of $MnFe_2O_4$ nanoparticles prepared at different pH values for RhB removal were examined using a batch adsorption experiment. Initially, at room temperature, 100 mg of the adsorbent was added to 100 mL of RhB reaction solution with a concentration of 2×10^{-5} M. During the adsorption process, samples were taken at 5 min intervals for 60 min. The $MnFe_2O_4$ nanoparticles were separated from the RhB solution by centrifugation at 3000 rpm for 5 min. The solute concentration was determined by a UV-vis spectrophotometer (Thermo Scientific Evolution 201) at λ_{max} = 550 nm. The adsorption capacity and removal efficiency were calculated using the following equations:[39,40]

$$q_e = \frac{(C_0 - C_e)V}{W} \quad (1)$$

$$E = \frac{(C_0 - C_e)}{C_0} \times 100\% \quad (2)$$

where q_e is the equilibrium adsorption capability (mg g^{-1}), C_0 and C_e are the initial and equilibrium concentrations of RhB (mg L^{-1}), W is the mass (g) of the magnetic adsorbent, and V is the volume of the solution (mL).

3. Results and discussion

3.1 Crystal structure

The XRD pattern of the $MnFe_2O_4$ powders prepared at different pH values are shown in Fig. 2. The considered diffraction peaks with 2θ values for $MnFe_2O_4$-pH 10.5 were 18.08°, 29.74°, 35.02°, 36.66°, 42.57°, 52.82°, 56.26°, and 61.74° corresponding to the crystal planes (111), (220), (311), (222), (400), (422), (511), and (440), respectively. According to the JCPDS standard (card no. 88–1965), the crystal structure of $MnFe_2O_4$ powders can be indexed as spinel structure belonging to the face center cubic (FCC) system. No diffraction peak was attributed to manganese

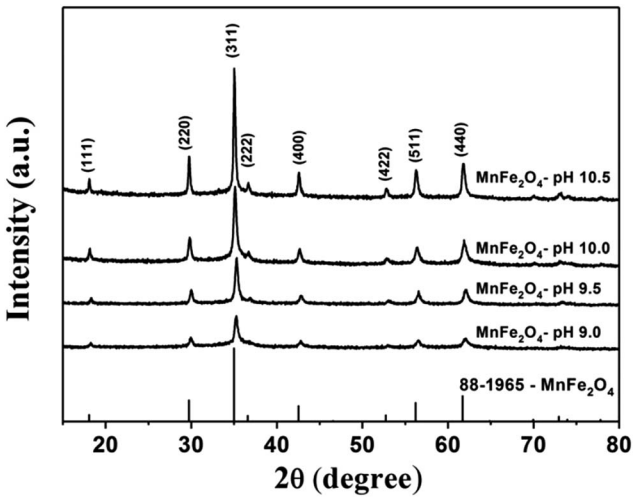

Fig. 2 XRD patterns of $MnFe_2O_4$ nanoparticles prepared by preparation by co-precipitation at the pH values of 9.0, 9.5, 10.0, and 10.5.

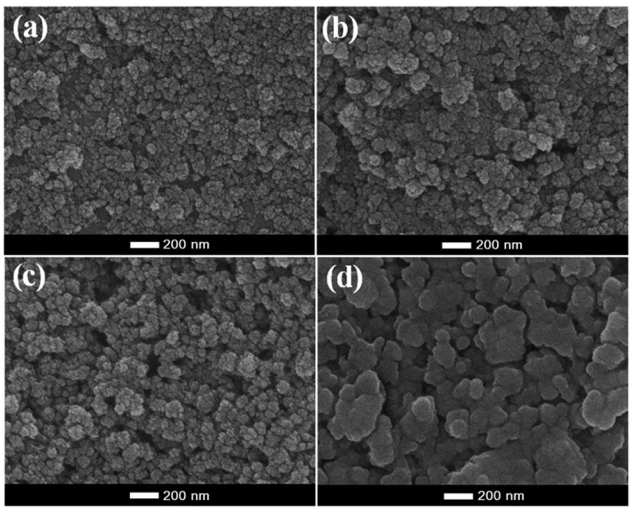

Fig. 3 SEM images of (a) $MnFe_2O_4$-pH 9.0, (b) $MnFe_2O_4$-pH 9.5, (c) $MnFe_2O_4$-pH 10.0 and (d) $MnFe_2O_4$-pH 10.5.

oxide and/or iron oxide materials. This suggests that the well-crystallized $MnFe_2O_4$ phase with a spinel structure has formed during the co-precipitation process.

As seen from Fig. 2, the XRD diffraction pattern of $MnFe_2O_4$-pH 9.0 shows the lowest intensity due to its small crystallite size with low crystallinity. On the other hand, the intensity of the (311) peak increased with increasing pH values from 9.5 to 10.5, indicating high crystallinity and large crystallite sizes for particles obtained under these preparation conditions. These results imply that the crystallite size and crystallinity of $MnFe_2O_4$ nanoparticles can be adjusted with the pH value used during the co-preparation process. The crystallite size of all samples was calculated using the Debye–Scherer formula.[41] The calculated crystallite size of $MnFe_2O_4$ at the pH values of 9.0, 9.5, 10.0, and 10.5 were 29.5, 41.2, 54.2, and 103.7 nm, respectively (Table 1).

3.2 Morphology

The morphology and particle size of $MnFe_2O_4$ nanoparticles with varying pH values (pH 9.0, 9.5, 10.0, and 10.5) were investigated by SEM and TEM images, and are shown in Fig. 3 and 4 as well as Table 1. Fig. 3 displays the SEM images of $MnFe_2O_4$ prepared at different pH values of 9.0, 9.5, 10.0, and 10.5. The images indicated that synthesized manganese ferrites were composed of agglomerated small particles. The morphology of $MnFe_2O_4$ nanoparticles appears to be not-so-hard-grained clusters. These nanoparticles consist of the spherical particles with average diameters of 69, 98, 149, and 247 nm for the preparation at pH values of 9.0, 9.5, 10.0, and 10.5, respectively. Furthermore, TEM images can reveal internal structures, and provide more accurate measurement of particle sizes and morphology. The morphology of $MnFe_2O_4$ nanoparticles from TEM images displayed spherical-like shapes. The average particle sizes of $MnFe_2O_4$ nanoparticles were 4.4, 4.5, 5.5, and 6.4 nm at the pH values 9.0, 9.5, 10.0, and 10.5, respectively (Fig. 4e–h). Fig. 4a–d show that the agglomerated particles diameter of $MnFe_2O_4$ increased as the pH value increased. The increase in the pH of the mixture solution resulted in more agglomeration of particles as the average particle size increased.[42,43] The agglomeration of $MnFe_2O_4$ nanoparticles affects the BET-specific surface area (SSA) (these results are shown in the Section 3.3 BET-specific surface area and pore size). The corresponding HRTEM images in Fig. 4i–l show lattice spacings of the $MnFe_2O_4$ nanoparticles prepared at pH 9.0 to 10.5. The d spacing of approximately 0.25 nm corresponds to the (311) plane of $MnFe_2O_4$.

3.3 BET-specific surface area and pore size

Fig. 5 shows the N_2 adsorption–desorption isotherms area and the pore size distribution of the as-prepared $MnFe_2O_4$ nanoparticles. The N_2 adsorption–desorption isotherm of $MnFe_2O_4$ nanoparticles was matched to a type IV hysteresis loop

Table 1 Physical properties of $MnFe_2O_4$ nanoparticles prepared by a co-precipitation at different pH values

$MnFe_2O_4$	XRD-crystallite size (nm)	TEM-particle size (nm)	SSA ($m^2\ g^{-1}$)	Average pore size diameter (nm)	M_s (emu g^{-1})
pH 9.0	29.5	4.4	182.82	2.934	24.58
pH 9.5	41.2	4.5	139.25	3.371	30.60
pH 10.0	54.2	5.5	157.59	3.849	36.72
pH 10.5	103.7	6.4	53.99	5.094	41.48

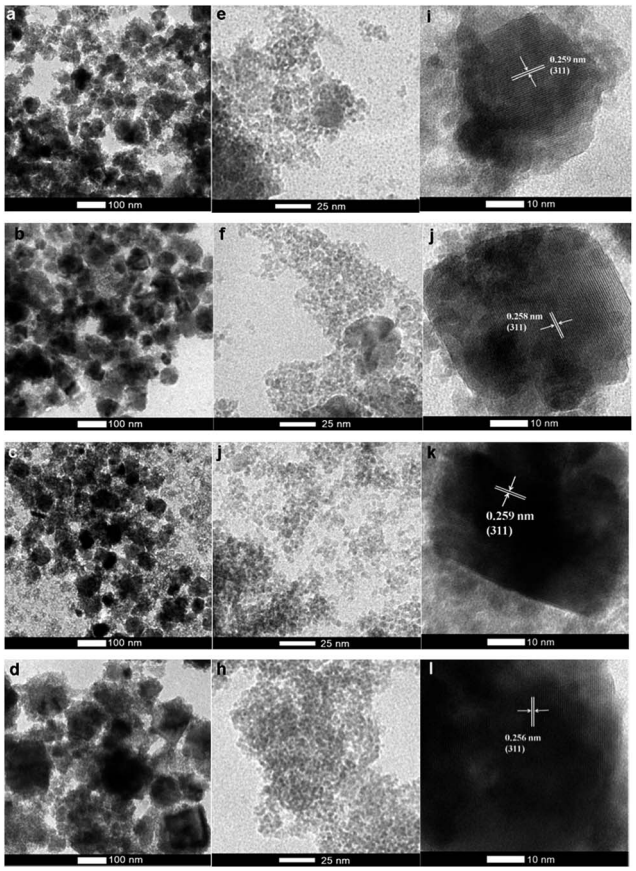

Fig. 4 TEM images and lattice fringes of $MnFe_2O_4$ nanoparticles prepared at the pH values of pH 9.0 (a, e and i), pH 9.5 (b, f and j), pH 10.0 (c, g and k), and pH 10.5 (d, h and l).

(according to the IUPAC classification) indicating a mesoporous structure. The BET-specific surface areas of the $MnFe_2O_4$ nanoparticles prepared at different pH values corresponded to the average pore size diameter as listed in Table 1. The $MnFe_2O_4$-pH 9.0 shows a specific surface area of 182.82 $m^2\ g^{-1}$ and increasing the pH to 10.5 shows a surface area notably diminished to 53.99 $m^2\ g^{-1}$. This is possibly because of the progressive aggregation of small crystallites into larger particles. The average pore size diameter was observed to increase as the pH increased. Furthermore, the most significant increase to a pore size of 5.094 nm was noted at the highest pH of 10.5. This result suggests that the larger pore size is beneficial to an improved ability of RhB to adsorb to the surface of $MnFe_2O_4$ nanoparticles. In addition to pore size of the adsorbent, other factors such as initial dye concentration and surface charge of the adsorbent influence the adsorption capacity of adsorbent materials.[43–46]

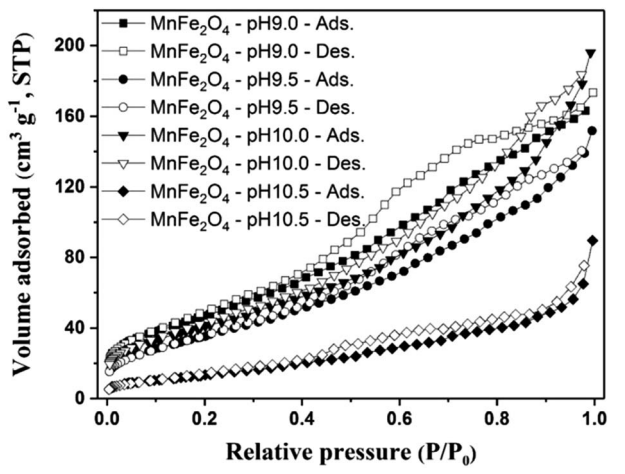

Fig. 5 N_2 adsorption–desorption isotherms for $MnFe_2O_4$ nanoparticles prepared at pH 9.0, 9.5, 10.0, and 10.5.

3.4 Magnetic properties

The magnetic properties of $MnFe_2O_4$ nanoparticles were investigated by using a vibrating sample magnetometer (VSM) at room temperature under magnetic fields up to ±10 kOe as shown in Fig. 6a. All $MnFe_2O_4$ samples exhibited soft magnetic behavior with a narrow hysteresis loop. The values of saturation magnetization (M_s) of $MnFe_2O_4$ nanoparticles prepared at pH 9.0, 9.5, 10.0, and 10.5 are shown in Table 1. The saturation magnetization of the $MnFe_2O_4$ nanoparticles increased as the increased pH value of the prepared $MnFe_2O_4$. $MnFe_2O_4$-pH 10.5 showed the highest M_s value (41.48 emu g^{-1}) due to the large magnetic dipole moments from the large particle size and the high crystallinity of the particles. The results also demonstrate a faster magnetic attraction by external magnetic field and probably a more effective removal of the $MnFe_2O_4$ particles from the large volume of water. In Fig. 6b, $MnFe_2O_4$-pH 10.5 was separated in solution after applying a magnetic field. It can be

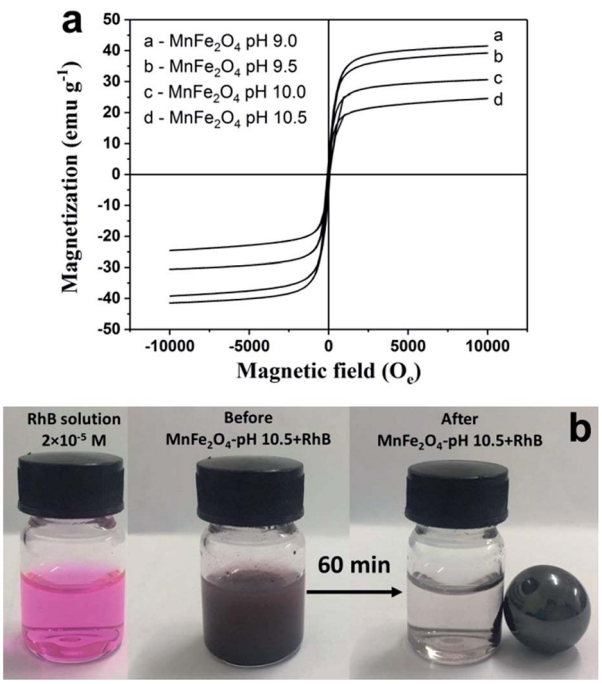

Fig. 6 (a) M–H curves of $MnFe_2O_4$ nanoparticles prepared at different pH values and (b) photograph of $MnFe_2O_4$ nanoparticles separation in RhB solution by using a magnet.

seen that the magnetic powders of $MnFe_2O_4$-pH 10.5 immediately moved towards the magnet and the RhB solution became clear.

3.5 Adsorption kinetics

In Fig. 7, the maximum removal percentage of RhB (96.92%) was observed for $MnFe_2O_4$-pH 10.5. The adsorption capacity of $MnFe_2O_4$ nanoparticles over RhB could be partially explained by the surface charges characterized by zeta potential. The point of zero charge (pzc) values of $MnFe_2O_4$ nanoparticles prepared at pH 9.0, 9.5, 10.0, and 10.5 were 5.58, 6.13, 6.69, and 5.18, respectively. The pH value of the suspension of the $MnFe_2O_4$ nanoparticles and RhB solution was measured to be approximately 8.8 which explains the negatives charges on the surface of the $MnFe_2O_4$. For this reason, the cationic RhB molecules would preferentially adsorb onto the negatively charged $MnFe_2O_4$ nanoparticles through electrostatic interaction.[47]

In order to further analyze the adsorption kinetics for removing RhB by $MnFe_2O_4$ nanoparticles, two kinetic models, the pseudo-first-order and pseudo-second-order, models, were applied. The adsorption capacities of $MnFe_2O_4$ nanoparticles for RhB adsorption are shown in Fig. 8a. The pseudo-first order equation is generally represented according the following equation[48,49] (eqn (3)):

$$\frac{dq_t}{dt} = k_1(q_e - q_t) \quad (3)$$

where k_1 and q_t are the rate constant of pseudo-first order kinetics (min^{-1}) and adsorption capacity at time t (min), respectively. After integration by applying the conditions, $q_t = 0$ at $t = 0$ and $q_t = q_t$ at $t = t$, the eqn (3) becomes

$$\log(q_e - q_t) = \log(q_e) - \left(\frac{k_1}{2.303}\right)t \quad (4)$$

The k_1, calculated q_e ($q_{e,\,cal}$), and correlation coefficients (R^2) of $MnFe_2O_4$ with varying pH values were determined as shown in Table 2. The plot of $\log(q_e - q_t)$ *versus* time after fitting the pseudo-first order model is presented in Fig. 8b. The $q_{e,\,cal}$ values of all samples were calculated from the intercept of the plot of $\log(q_e)$ *versus* t. From the obtained data, R^2 was relatively low, indicating that the pseudo-first order model was not well suited to predict the kinetic rate constant. Therefore, the pseudo-second order model was applied to determine the

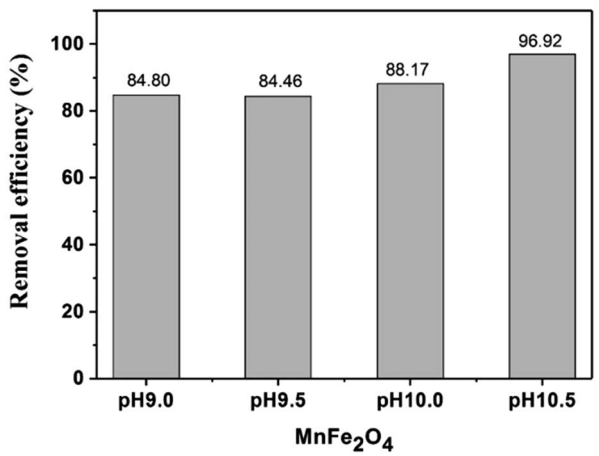

Fig. 7 Removal efficiency of RhB by $MnFe_2O_4$ nanoparticles prepared by co-precipitation at different pH values.

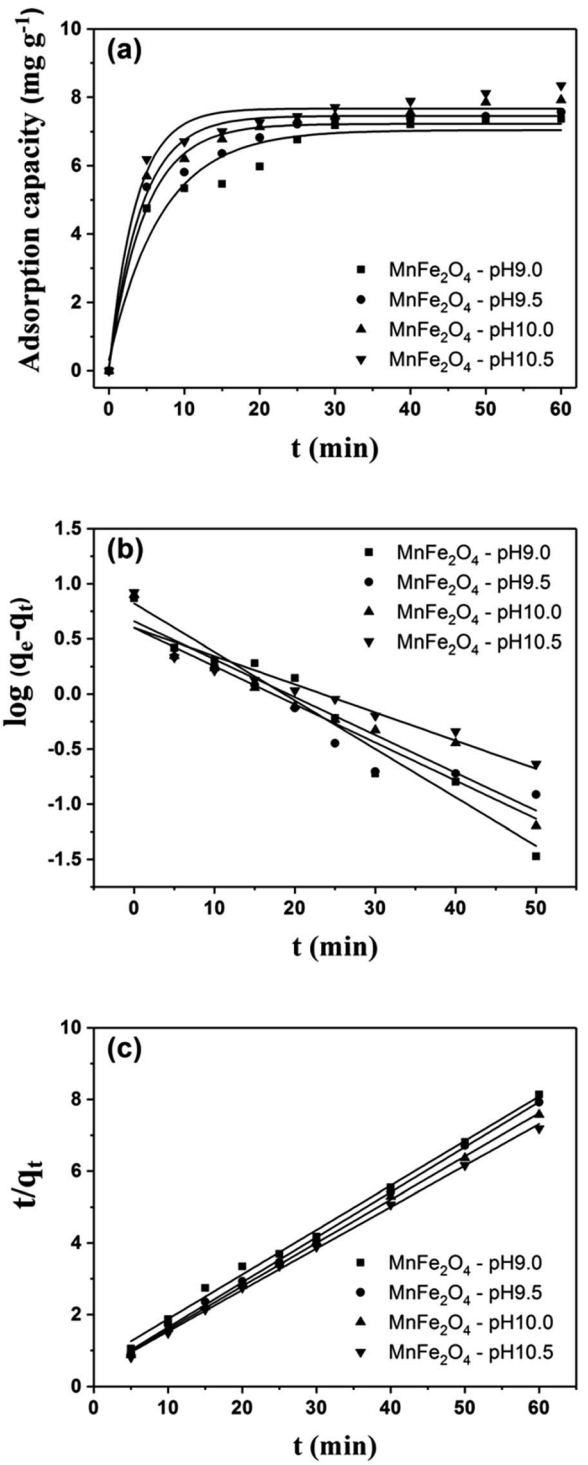

Fig. 8 Adsorption kinetics of (a) $MnFe_2O_4$, the plots of (b) pseudo-first order, and (c) pseudo-second order kinetic models for RhB adsorption onto $MnFe_2O_4$ nanoparticles with varying pH preparation values.

Table 2 Kinetic parameters, q_e, $q_{e,\,cal}$, k_1, k_2, and correlation of coefficient R^2 for the adsorption of RhB onto $MnFe_2O_4$ nanoparticles prepared at varying pH values

		Pseudo-first order			Pseudo-second order		
Samples	q_e (mg g^{-1})	$q_{e,\,cal}$ (mg g^{-1})	k_1 (min^{-1})	R^2	$q_{e,\,cal}$ (mg g^{-1})	k_2 (g mg^{-1} min^{-1})	R^2
$MnFe_2O_4$-pH 9.0	7.37	6.61	0.101	0.9587	7.76	0.283	0.9916
$MnFe_2O_4$-pH 9.5	7.57	3.97	0.079	0.9143	7.78	0.469	0.9975
$MnFe_2O_4$-pH 10.0	7.92	4.55	0.078	0.9295	8.10	0.460	0.9976
$MnFe_2O_4$-pH 10.5	8.35	3.97	0.059	0.8975	8.45	0.443	0.9967

suitable kinetic model which is expressed as the following equation:

$$\frac{dq_t}{dt} = k_2(q_e - q_t) \quad (5)$$

where k_2 is the pseudo-second order rate constant (g mg^{-1} min^{-1}). After integrating eqn (5), the linear fitting is expressed as the following equation:

$$\frac{t}{q_t} = \frac{1}{k_2 q_e^2} + \frac{t}{q_e} \quad (6)$$

Fig. 8c shows pseudo-second-order kinetic models for RhB adsorption onto $MnFe_2O_4$ nanoparticles with varying pH preparation values. The adsorption kinetics and parameters of k_2 and $q_{e,\,cal}$ from the intercept and slope of the plot of t/q_t *versus* t are shown in Table 2. The R^2 values show that the RhB removal kinetics can be approximated using a pseudo-second order model. Thus, the pseudo-second order model is more appropriate for explaining this adsorption process.

3.6 Adsorption isotherms

Two adsorption isotherm models, Langmuir and Freundlich equations, were used to further describe the adsorption equilibrium. The Langmuir equation describes monolayer adsorption with limited homogeneous sites. The Langmuir model is given by the following equation:[50,51]

$$q_e = \frac{q_m K_L C_e}{(1 + K_L C_e)} \quad (7)$$

where C_e, K_L, q_e, q_m, are the concentration of adsorbate at equilibrium (mg L^{-1}), Langmuir constant (L mg^{-1}), the amount of solute adsorbed at the equilibrium of RhB (mg g^{-1}), and the maximum adsorption capacity of RhB (mg g^{-1}), respectively. Eqn (7) can be expressed in a linear form as displayed in the following equation:

$$\frac{C_e}{q_e} = \frac{1}{K_L q_m} + \frac{C_e}{q_m} \quad (8)$$

Fig. 9a shows linear forms of the isotherms for representative RhB adsorption by $MnFe_2O_4$ nanoparticles with varying preparation of pH values. The Langmuir isotherm for RhB adsorption on $MnFe_2O_4$ nanoparticles was examined from a linear plot of C_e/q_e *versus* C_e as presented in Fig. 9b.

The Freundlich isotherm is one of the applicable models to describe heterogeneous surface adsorption and multilayer adsorption under various non-ideal conditions. The Freundlich

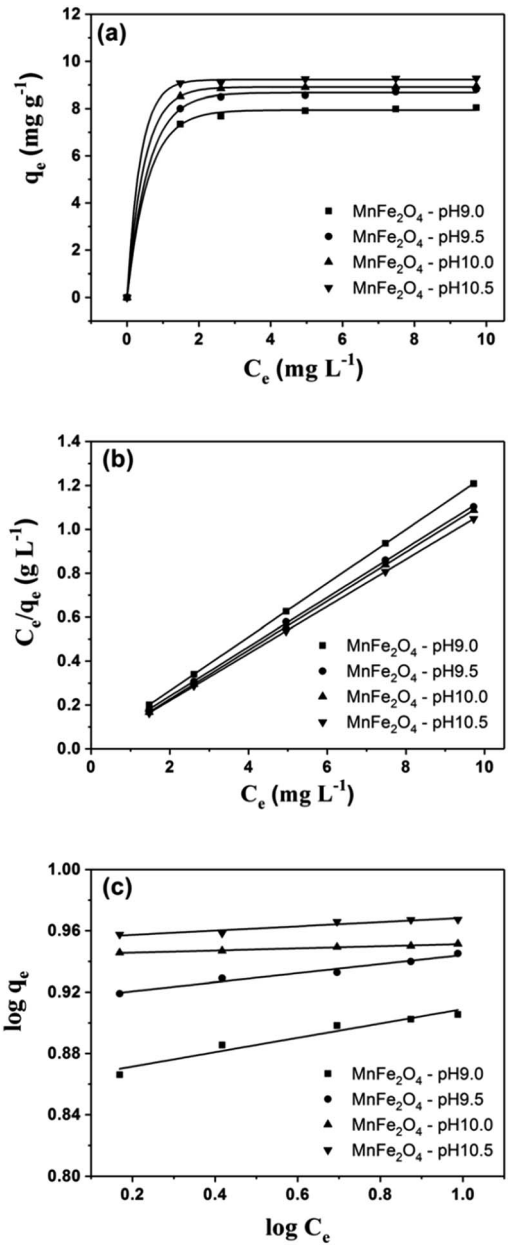

Fig. 9 (a) Adsorption isotherms, (b) a typical linear Langmuir, and (c) Freundlich isotherms of RhB removal using $MnFe_2O_4$ nanoparticles with varying pH preparation values.

Table 3 Extracted values of q_m, K_L, K_f, and n from RhB adsorption using $MnFe_2O_4$ nanoparticles by curve fitting based on Langmuir and Freundlich isotherms

		Langmuir equation			Freundlich equation		
Samples	q_e (mg g^{-1})	q_m (mg g^{-1})	K_L (L mg^{-1})	R^2	K_f (L mg^{-1})	$1/n$	R^2
$MnFe_2O_4$-pH 9.0	8.04	8.09	10.75	0.9998	7.28	0.0469	0.9052
$MnFe_2O_4$-pH 9.5	8.81	8.83	13.33	0.9998	8.22	0.0295	0.9688
$MnFe_2O_4$-pH 10.0	8.94	8.94	22.82	0.9999	8.80	0.0170	0.9869
$MnFe_2O_4$-pH 10.5	9.28	9.30	34.68	0.9999	9.01	0.0139	0.9139

isotherm can be shown in the simplest model[50,51] as the following:

$$q_e = K_F C_e^{\frac{1}{n}} \quad (9)$$

where K_F and $1/n$ are the adsorption capacity at unit concentration (L mg^{-1}) and adsorption intensity, respectively. The $1/n$ indicates the degree of non-linearity between solution concentration and adsorption, $1/n = 0$ (irreversible), $0 < 1/n < 1$ (favorable), and $1/n > 1$ (unfavorable). The linear form of the Freundlich isotherm can be expressed as the following equation:

$$\log q_e = \log K_F + \frac{1}{n}\log C_e \quad (10)$$

The values of K_F, n, and R^2 are shown in Table 3. The fitting result of the Freundlich model using eqn (10) for RhB adsorption on $MnFe_2O_4$ nanoparticles is shown in Fig. 9c. From the fitting results of the Langmuir and Freundlich models, the experiment isotherm fits quite well with the Langmuir model based on an examination of the values of each model's constant and correlation coefficient (R^2). This implies that the RhB adsorption onto $MnFe_2O_4$ is monolayer adsorption and the adsorption sites of $MnFe_2O_4$ nanoparticles are homogeneous. Moreover, the practical value of the equilibrium adsorption ability is much closer to the theoretical value obtained from the Langmuir model.

The adsorption capacity of the as-prepared $MnFe_2O_4$ nanoparticles was compared with other reports as shown in Table 4.[52–57] It was found that the adsorption capacity of adsorbents depends on several factors such as size, morphology, and specific surface area. Moreover, the extrinsic properties of adsorption capacity such as adsorbent loading and initial dye concentration significantly affected to the removal efficiency. No report has been found for $MnFe_2O_4$ reacting with RhB from previous work (Table 5).[58–63] It was found that $MnFe_2O_4$ nanoparticles can adsorb RhB from water with adsorption capacity of 9.30 mg g^{-1}. This indicates that the prepared $MnFe_2O_4$ nanoparticles can be considered as a promising adsorbent for the removal of rhodamine B from aqueous solution.

3.7 Fourier transform infrared analysis

The FTIR spectroscopy was performed to investigate the possible interactions between $MnFe_2O_4$ nanoparticles and RhB as shown in Fig. 10. The $MnFe_2O_4$-pH 10.5 exhibits an adsorption peak at 1624 cm^{-1}, corresponding to O–H group due to the adsorbed water or moisture in samples. The broad band at around 3392 cm^{-1} is attributed to the symmetric vibration of –OH groups of H_2O adsorbed by the sample. Meanwhile, the two bands at 576 and 1384 cm^{-1} can be attributed to the intrinsic vibrations of octahedral coordinated metal ions in the spinel structure and OH bending vibration, respectively. Typically, the metal oxide vibrations occur below 1000 cm^{-1}.[64,65] For spectrum of RhB, the weak intensity band at 2983 cm^{-1} is associated with the aromatic C–H vibrations, which also appear at 1130 cm^{-1} (plane bending) and at 682 cm^{-1} (wagging vibrations). Moreover, the vibration bands in 2928–2869 cm^{-1} is inferred to the presence of RhB. In addition, the band at 1696 cm^{-1} corresponds to the C=O stretching vibration, while the band at 1341 cm^{-1} is associated with aromatic skeletal C–C

Table 4 Comparison of the studied dyes with $MnFe_2O_4$ and $MnFe_2O_4$-based composites as adsorbents based on the removal capacities

	Properties			Adsorption properties				
Adsorbent	Size (nm)	SSA (m^2 g^{-1})	M_s (emu g^{-1})	Dye	Initial dye concentration (mg L^{-1})	Adsorbent loading (g L^{-1})	q_e (mg g^{-1})	Reference
$MnFe_2O_4$	80–100	—	78.4	Congo red	100	0.3	92.4	52
$MnFe_2O_4$	200–290	155.7	18.8	Congo red	150	16	25.78	53
$MnFe_2O_4$	2470	68.6	42.8	Azo dye acid red B	100	4	53.8	54
$MnFe_2O_4$/bentonite	300–800	130	—	AR138	100	0.1 g/30 ml	—	55
$MnFe_2O_4$/PW	21.1–25.6	—	1.53	Congo red	50–100	0.05–0.1 g	86.96	56
$MnFe_2O_4$@resin	<5 (TEM)	—	6.2	Congo red	10	0.2	1000	57
$MnFe_2O_4$	5	53.99	41.48	RhB	7.5	0.1	9.30	In this study

Table 5 Comparison of the studied RhB with different types of adsorbents based on the adsorption capacities

	Properties			Adsorption properties				
Adsorbent	Size (nm)	SSA ($m^2\ g^{-1}$)	M_s (emu g^{-1})	Dye	Initial dye concentration (mg L^{-1})	Adsorbent loading (g L^{-1})	q_e (mg g^{-1})	Reference
Fly ash	7500	40.16	40.16	RhB	5–25	20	0.193–0.173	58
$ZnFe_2O_4$	4–13	139	139	RhB	5–25	0.15	5.02–9.38	59
$ZnTi_{0.6}Fe_{1.4}O_4$	20	—	—	RhB	4–36	0.05–2.0	~8–17	60
$BiFeO_3$	60–80	—	—	RhB	25	0.5 g	64.22	61
$CoFe_2O_4$/graphene oxide	14.58	239.76	59.2	RhB	3.75	0.25	121.8	62
Graphene/Fe_3O_4	<50	—	—	RhB	20	0.6	30.211	63
$MnFe_2O_4$	5	53.99	41.48	RhB	7.5	0.1	9.30	In this study

stretch.[66–68] The appearances of the three peaks at 2961, 2920, 2855 cm^{-1} after RhB adsorption could be attributed to the formation of chemical bonds between RhB and $MnFe_2O_4$. These peaks shifted after RhB adsorption, confirming the interactions between $MnFe_2O_4$ and RhB.[32,69]

3.8 UV-vis and XPS analyses

The adsorption mechanism of the $MnFe_2O_4$-pH 10.5 to remove RhB was investigated using UV-vis absorption spectroscopy and X-ray photoelectron spectroscopy (XPS) techniques. From Fig. 11a, the characteristic peak of RhB appeared on the spectrum of $MnFe_2O_4$/RhB. This peak signifies that RhB was absorbed on the surface of the $MnFe_2O_4$ nanoparticles. In Fig. 11b, the two peaks of Mn 2p, centered at about 641 and 653 eV, correspond to the binding energy for Mn $2p_{3/2}$ and Mn $2p_{1/2}$, indicating the oxidation state of Mn^{2+} in $MnFe_2O_4$ nanoparticles.[70,71] Moreover, the Fe 2p spectra show two main peaks at the binding energies of about 711 and 724 eV, which are assigned to the Fe $2p_{3/2}$, and Fe $2p_{1/2}$ of Fe^{3+}, respectively (Fig. 11c).[72,73] The interaction of RhB and $MnFe_2O_4$ nanoparticles at the interface was also determined by XPS technique. The N 1s spectra of $MnFe_2O_4$ nanoparticles after RhB adsorption were contributed to the components of $-NH_2$ (~401 eV) and –NH (~399 eV) (Fig. 11d).[74,75] The N 1s peaks appearing in the spectrum of the $MnFe_2O_4$ nanoparticles/RhB while disappearing in the $MnFe_2O_4$ nanoparticles. Therefore, this indicates the presence RhB on the surface of the $MnFe_2O_4$ nanoparticles. The O 1s deconvoluted spectrum of $MnFe_2O_4$ nanoparticles before RhB adsorption (Fig. 11e) presents four Gaussian peaks centered at 529.92, 531.13, 531.98, and 532.99–534.12 eV associated with the binding energies of the lattice oxygen species (O^{2-}), highly oxidative oxygen species (O_2^{2-}/O^-), hydroxyl groups (–OH), and surface adsorbed water molecules (H_2O), respectively.[69,76,77] The XPS spectrum of the O 1s shows a chemical shift after adsorption of RhB onto the $MnFe_2O_4$ surface. This is attributed to the adsorption of RhB on the surface of

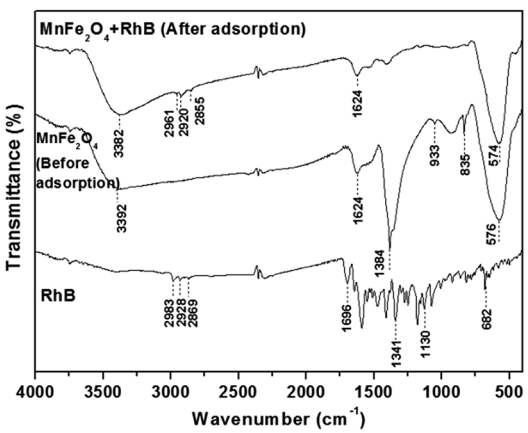

Fig. 10 FTIR spectra of RhB and $MnFe_2O_4$-pH 10.5 before and after RhB adsorption.

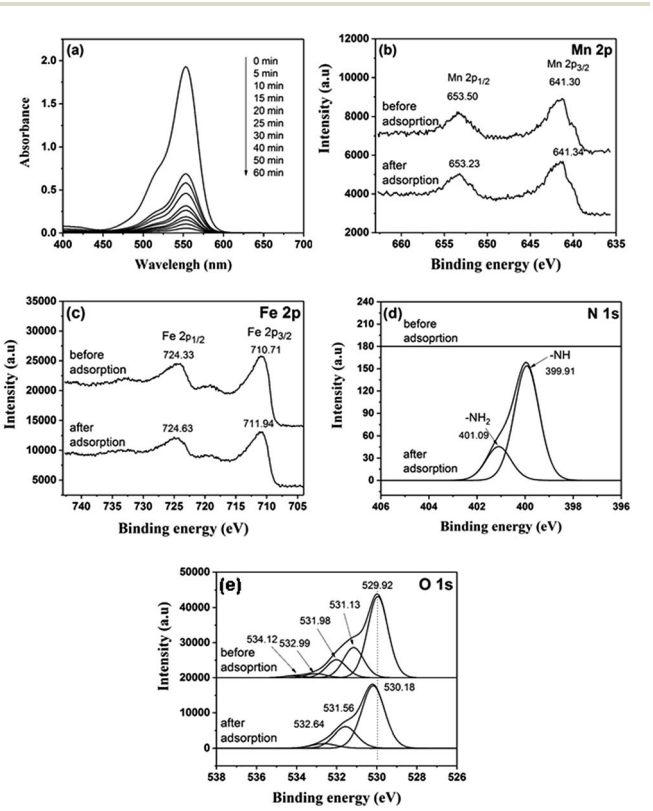

Fig. 11 (a) UV-visible absorption spectra of $MnFe_2O_4$ prepared at pH of 10.5 with different adsorption times of RhB adsorption in aqueous solution. XPS spectra of $MnFe_2O_4$ microspheres before and after RhB adsorption. Peak-fitting XPS spectra in the (b) Mn 2p, (c) Fe 2p, (d) N 1s, and (e) O 1s regions of $MnFe_2O_4$ nanoparticles and $MnFe_2O_4$/RhB.

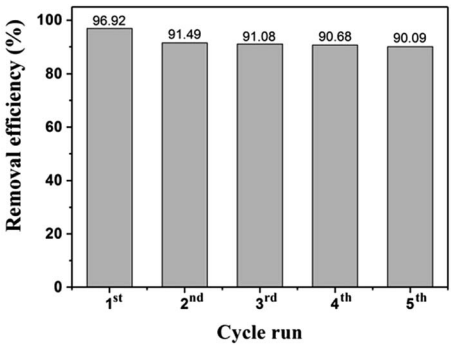

Fig. 12 Removal efficiencies of RhB during adsorption cycles for $MnFe_2O_4$-pH 10.5.

$MnFe_2O_4$ particles.[78,79] The significant binding energy shifts observed from XPS study as well as the results from UV-vis and zeta potential analyses suggest there is strong electrostatic and chemical interactions between $MnFe_2O_4$ and RhB. These results confirm the adsorption of RhB on the $MnFe_2O_4$ surface.

3.9 Reusability of $MnFe_2O_4$ nanoparticles

Reusability is one of the prerequisites to verify the practicality of a direct application of adsorbents for dye removal. The stability of the $MnFe_2O_4$-pH 10.5 was evaluated by repeating experiments on the RhB adsorption as shown in Fig. 12.

After each run, the $MnFe_2O_4$ nanoparticles were collected using a magnetic field and washed by ultrasonic cleaning with deionized water following with absolute ethanol. Then, the separated $MnFe_2O_4$ nanoparticles were re-dispersed in fresh RhB solution with the same concentration (2×10^{-5} M), and next the new adsorption cycle began again. After 5 cycles, the removal efficiency decreased by a small fraction from 96.92% to 90.09%.

4. Conclusions

The magnetically separable $MnFe_2O_4$ nanoparticles were successfully prepared by a co-precipitation method with varying pH values. It was found that the physical, magnetic, and adsorption properties of $MnFe_2O_4$ nanoparticles were changed by controlling the pH value during $MnFe_2O_4$ nanoparticles preparation. The $MnFe_2O_4$-pH 10.5 sample exhibited the highest adsorption capacity towards RhB solution. The highest adsorption of RhB on the $MnFe_2O_4$-pH 10.5 sample depends on two factors that are large pore size and negative charge surface. Moreover, the reusability of $MnFe_2O_4$-pH 10.5 particles can be achieved by an external magnetic field separation with magnetization of 41.48 emu g^{-1}. The experimental results correlated reasonably well with the Langmuir model. The adsorption kinetics of RhB by $MnFe_2O_4$ followed the pseudo-second order model. This study concludes that the facile synthesized magnetic $MnFe_2O_4$ nanoparticles prove to be effective as a potential adsorbent for the removal of RhB from aqueous solutions and a promising adsorbent for further utilizations in dye removal from colored textile wastewater.

Conflicts of interest

There are no conflicts to declare.

Acknowledgements

We wish to thank the following organizations for financial support: the Thailand Graduate Institute of Science and Technology Development Agency (TGIST), National Science and Technology Development Agency (NSTDA); the Center of Excellence in Materials Science and Technology, Chiang Mai University under the administration of Materials Science Research Center, Faculty of Science and the Graduate School, Chiang Mai University. Finally, we would like to thank Ms. Cythia Bail for her grateful kindness and valuable guidance for manuscript preparation.

References

1 S. Zhu, T. Xu, H. Fu, J. Zhao and Y. Zhu, *Environ. Sci. Technol.*, 2007, **41**, 6234.
2 P. Saritha, C. Aparna, V. Himabindu and Y. Anjaneyulu, *J. Hazard. Mater.*, 2007, **149**, 609.
3 S. C. Jung, *Water Sci. Technol.*, 2011, **63**(7), 1491.
4 T. Yao, S. Guo, C. Zeng, C. Wang and L. Zhang, *J. Hazard. Mater.*, 2015, **292**, 90.
5 Q. Li, Q. Yue, Y. Su, B. Gao and J. Li, *J. Hazard. Mater.*, 2009, **165**, 1170.
6 E. Baldev, D. Mubarakali, A. Ilavarasi, D. Pandiaraj, K. A. Sheik Syed Ishack and N. Thajuddin, *Colloids Surf., B*, 2013, **105**, 207.
7 I. K. Konstantinou and T. A. Albanis, *Appl. Catal., B*, 2004, **49**, 1.
8 H. Lee, S. H. Park, Y.-K. Park, B. H. Kim, S.-J. Kim and S.-C. Jung, *Chem. Cent. J.*, 2013, 7(156), 1.
9 C. Galindo, P. Jacques and A. Kalt, *Chemosphere*, 2001, **45**, 997.
10 W. S. Kuo and P. H. Ho, *Chemosphere*, 2001, **45**, 77.
11 A. Y. Zahrim and N. Hilal, *Water Resources and Industry*, 2014, **3**, 23.
12 S. A. Avlonitis, I. Poulios, D. Sotiriou, M. Pappas and K. Moutesidis, *Desalination*, 2008, **221**, 259.
13 Q. Y. Yue, B. Y. Gao, Y. Wang, H. Zhang, X. Sun, S. G. Wang and R. R. Gu, *J. Hazard. Mater.*, 2008, **152**, 221.
14 S. Wang, *Dyes Pigm.*, 2008, **76**, 714.
15 M. Sundrarajan, G. Vishnu and K. Joseph, *Dyes Pigm.*, 2007, **75**, 273.
16 J. Liu, S. Ma and L. Zang, *Appl. Surf. Sci.*, 2013, **265**, 393.
17 H. Tajizadegan, M. Jafari, M. Rashidzadeh and A. Saffar-Teluri, *Appl. Surf. Sci.*, 2013, **276**, 317.
18 W. Deligeer, Y. W. Gao and S. Asuha, *Appl. Surf. Sci.*, 2011, **257**, 3524.
19 M. Anbia, S. Asl Hariri and S. N. Ashrafizadeh, *Appl. Surf. Sci.*, 2010, **256**, 3228.
20 J. Hu, I. M. C. Lo and G. Chen, *Langmuir*, 2005, **21**, 11173.
21 H. F. Liang and Z. C. Wang, *Mater. Chem. Phys.*, 2010, **124**, 964.

22 S. Zhang, H. Niu, Y. Cai, X. Zhao and Y. Shi, *Chem. Eng. J.*, 2010, **158**, 599.
23 X. Bao, Z. Qiang, W. Ling and J. Chang, *Sep. Purif. Technol.*, 2013, **117**, 104.
24 J. G. Parsons, M. L. Lopez, J. R. Peralta-Videa and J. L. Gardea-Torresdey, *Microchem. J.*, 2009, **91**, 100.
25 J. Dui, G. Zhu and S. Zhou, *ACS Appl. Mater. Interfaces*, 2013, **5**, 10081.
26 I. Ibrahim, I. O. Ali, T. M. Salama, A. A. Bahgat and M. M. Mohamed, *Appl. Catal., B*, 2016, **181**, 389.
27 D. Chen, Y. Zhang and Z. Kang, *Chem. Eng. J.*, 2013, **215–216**, 235.
28 W. Wang, Z. Ding, M. Cai, H. Jian, Z. Zeng, F. Li and J. P. Liu, *Appl. Surf. Sci.*, 2015, **346**, 348.
29 Y. Ren, N. Li, J. Feng, T. Luan, Q. Wen, Z. Li and M. Zhang, *J. Colloid Interface Sci.*, 2012, **367**, 415.
30 X. Hou, J. Feng, X. Xu and M. Zhang, *J. Alloys Compd.*, 2010, **491**, 258.
31 M. P. Reddy, A. M. A. Mohamed, M. V. Ramana, X. B. Zhou and Q. Huang, *J. Magn. Magn. Mater.*, 2015, **395**, 185.
32 X. Hou, J. Feng, Y. Ren, Z. Fan and M. Zhang, *Colloids Surf., A*, 2010, **363**, 1.
33 M. Augustin and T. Balu, *Mater. Today*, 2015, **2**, 923.
34 C. Pereira, A. M. Pereira, C. Fernandes, M. Rocha, R. Mendes, M. P. Fernández-García, A. Guedes, P. B. Tavares, J.-M. Grenèche, J. P. Araújo and C. Freire, *Chem. Mater.*, 2012, **24**, 1496.
35 M. J. Akhta and M. Younas, *Solid State Sci.*, 2012, **14**, 1536.
36 N. S. Gajbhiye and G. Balaji, *Thermochim. Acta*, 2002, **385**, 143–151.
37 J. Wang, T. Deng, Y. Lin, C. Yang and W. Zhan, *J. Alloys Compd.*, 2008, **450**, 532.
38 M. Vadivel, R. R. Babu, K. Sethuraman, K. Ramamurthi and M. Arivanandhan, *J. Magn. Magn. Mater.*, 2014, **362**, 122.
39 Y. Xiao, H. Liang, W. Chen and Z. Wang, *Appl. Surf. Sci.*, 2013, **285**, 498.
40 X. Fang, J. Xiao, S. Yang, H. He and C. Sun, *Appl. Catal., B*, 2015, **162**, 544.
41 T. Huang, S. Mao, J. Yu, Z. Wen, G. Lu and J. Chen, *RSC Adv.*, 2013, **3**, 16657.
42 A. Molea, V. Popescu, N. A. Rowson and A. M. Dinescu, *Powder Technol.*, 2014, **253**, 22.
43 J. Jaramillo, B. A. Garzón and L. TiradoMejía, *J. Phys.: Conf. Ser.*, 2016, **687**, 12.
44 Q. Hu, Y. Liu, X. Gu and Y. Zhao, *Chemosphere*, 2017, **181**, 328.
45 S. Zhang, H. Niu, Y. Cai, X. Zhao and Y. Shi, *Chem. Eng. J.*, 2010, **158**, 599.
46 M. Iram, C. Guo, Y. Guan, A. Ishfaq and H. Liu, *J. Hazard. Mater.*, 2010, **181**, 1039.
47 S. Wang, X. Zhang, L. Pan, F.-M. Zhao, J.-J. Zou, T. Zhang and L. Wang, *Appl. Catal., B*, 2015, **64**, 234.
48 L. Wang, J. Li, Y. Wang, L. Zhao and Q. Jiang, *Chem. Eng. J.*, 2012, **181–182**, 72.
49 Y.-S. Ho, *J. Hazad. Mater.*, 2006, **136**, 681.
50 Y. C. Wong, Y. S. Szeto, W. H. Cheung and G. McKay, *Langmuir*, 2003, **19**, 7888.
51 G. A. Sayğili, *J. Mol. Liq.*, 2015, **211**, 515.
52 L. Wang, J. Li, Y. Wang, L. Zhao and Q. Jiang, *Chem. Eng. J.*, 2012, **181–182**, 72.
53 L. Yang, Y. Zhang, X. Liu, X. Jiang, Z. Zhang, T. Zhang and L. Zhang, *Chem. Eng. J.*, 2014, **246**, 88.
54 R. Wu and J. Qu, *J. Chem. Technol. Biotechnol.*, 2005, **80**, 20.
55 S. Hashemian, *Afr. J. Biotechnol.*, 2010, **9**(50), 8667.
56 G. A. Sayğılı, *J. Mol. Liq.*, 2015, **211**, 515.
57 M. H. Beyki, H. Alijani and Y. Fazli, *J. Mol. Liq.*, 2016, **216**, 6.
58 T. A. Khan, I. Ali, V. Vati Singh and S. Sharma, *J. Environ. Prot.*, 2009, **3**, 11.
59 W. Konicki, D. Siber and U. Narkiewicz, *Pol. J. Chem. Technol.*, 2017, **19**(4), 65.
60 J. Feng, Y. Hou, Y. Wang, X. Wang, H. Chen and L. Li, *Sci. China: Chem.*, 2016, **59**, 1033.
61 T. Soltani and M. H. Entezari, *Chem. Eng. J.*, 2013, **223**, 145.
62 W. Yin, S. Hao and H. Cao, *RSC Adv.*, 2017, **7**, 4062.
63 M. Mehrali, E. Sadeghinezhad, A. R. Akhiani, S. T. Latibari, H. S. C. Metselaar, A. S. Kherbeet and M. Mehrali, *Powder Technol.*, 2017, **308**, 149.
64 S. Kanagesan, S. B. A. Aziz, M. Hashim, I. Ismail, S. Tamilselvan, N. B. B. M. Alitheen, M. K. Swamy and B. P. C. Rao, *Molecules*, 2016, **21**, 312.
65 P. Iranmanesh, S. Saeednia, M. Mehran and S. Rashidi Dafeh, *J. Magn. Magn. Mater.*, 2017, **425**, 31.
66 D. Zhao, C. Chen, Y. Wang, W. Ma, J. Zhao, T. Rajh and L. Aang, *Environ. Sci. Technol.*, 2008, **42**, 308.
67 Q. He, J. Shi, X. Cui, J. Zhao, Y. Chen and J. Zhou, *J. Mater. Chem.*, 2009, **19**, 3395.
68 R. M. Dukali, I. M. Radović, D. B. Stojanović, D. M. Šević, V. J. Radojević, D. M. Jocić and R. R. Aleksić, *J. Serb. Chem. Soc.*, 2014, **79**(7), 867.
69 J. Fu, Q. Xin, X. Wu, Z. Chen, Y. Yan, S. Liu, M. Wang and Q. Xu, *J. Colloid Interface Sci.*, 2016, **461**, 292.
70 Q. Tang, L. Jiang, J. Liu, S. Wang and G. Sun, *ACS Catal.*, 2014, **4**, 457.
71 J. Chen, W. Wen, L. Kong, S. Tian, F. Ding and Y. Xiong, *Ind. Eng. Chem. Res.*, 2014, **56**, 6297.
72 Y. Yao, Y. Cai, F. Lu, F. Wei, X. Wang and S. Wang, *J. Hazard. Mater.*, 2014, **270**, 61.
73 Z. Zhang, Y. Wang, Q. Tan, Z. Zhong and F. Su, *J. Colloid Interface Sci.*, 2013, **398**, 185.
74 J. Zhang, T. Yao, C. Guan, N. Zhang, H. Zhang, X. Zhang and J. Wu, *J. Colloid Interface Sci.*, 2017, **505**, 130.
75 L. Chen, F. He, N. Zhao and R. Guo, *Appl. Surf. Sci.*, 2017, **420**, 669.
76 F.-T. You, G.-W. Yua, Y. Wang, Z.-J. Xing, X.-J. Liu and J. Li, *Appl. Surf. Sci.*, 2017, **413**, 387.
77 Y. J. Oh, J. J. Yoo, Y. I. Kim, J. K. Yoon, H. N. Yoon, J.-H. Kim and S. B. Park, *Electrochim. Acta*, 2014, **116**, 118.
78 T. Serizawa, H. Takeshita and M. Akashi, *Langmuir*, 1998, **14**, 4088.
79 S. Banerjee and M. C. Chattopadhyaya, *Arabian J. Chem.*, 2017, **10**, S1629.

